

GS-ProCams: Gaussian Splatting-based Projector-Camera Systems

Qingyue Deng¹, Jijiang Li¹, Haibin Ling², Bingyao Huang¹

¹Southwest University

²Stony Brook University

{qingyue@email., jijiangli@email., bhuang@}swu.edu.cn, hling@cs.stonybrook.edu

Abstract

We present *GS-ProCams*, the first Gaussian Splatting-based framework for projector-camera systems (*ProCams*). *GS-ProCams* significantly enhances the efficiency of projection mapping (PM) that requires establishing geometric and radiometric mappings between the projector and the camera. Previous CNN-based *ProCams* are constrained to a specific viewpoint, limiting their applicability to novel perspectives. In contrast, NeRF-based *ProCams* support view-agnostic projection mapping, however, they require an additional colocated light source and demand significant computational and memory resources. To address this issue, we propose *GS-ProCams* that employs 2D Gaussian for scene representations, and enables efficient view-agnostic *ProCams* applications. In particular, we explicitly model the complex geometric and photometric mappings of *ProCams* using projector responses, the target surface’s geometry and materials represented by Gaussians, and global illumination component. Then, we employ differentiable physically-based rendering to jointly estimate them from captured multi-view projections. Compared to state-of-the-art NeRF-based methods, our *GS-ProCams* eliminates the need for additional devices, achieving superior *ProCams* simulation quality. It is also 600 times faster and uses only 1/10 of the GPU memory.

1. Introduction

Projector-camera systems (*ProCams*) are integrated systems that combine a projector and a camera, and have emerged as indispensable tools in computer vision [3, 5, 43, 44, 60, 61, 76], spatial augmented reality (SAR)/projection mapping (PM) [12–15, 22, 30, 48, 56, 57, 62, 66, 67], providing exceptional experiences in immersive interaction, artistic creation and exhibition, as well as industrial design and manufacturing, among other domains.

Geometric and photometric mappings between the projector and the camera, which are foundational to *ProCams*, serve as cornerstones for numerous applications. For exam-

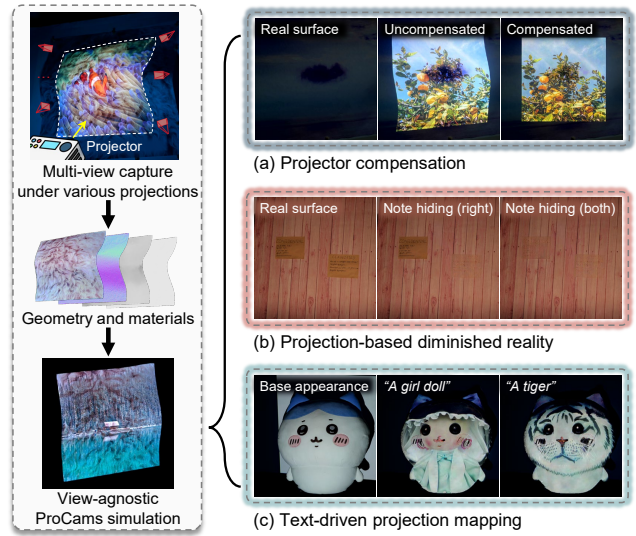


Figure 1. **GS-ProCams**. We represent the scene using 2D Gaussian, allowing us to efficiently model the geometric and photometric mappings of *ProCams*. By projecting various patterns onto the target surface and capturing images from multiple viewpoints using a camera, we achieve high-fidelity *ProCams* simulation while estimating the target surface’s geometry and materials. After training on a scene, *GS-ProCams* can achieve efficient view-agnostic (a) projector compensation, (b) projection-based diminished reality [29, 45] (with inpainting models [65]), and (c) projection mapping [28] (with diffusion models [21, 53]).

ple, structured light utilizes the geometric and photometric constraints of *ProCams* to estimate the object geometry and materials [18, 39, 54, 55]. Furthermore, by *ProCams* geometric correction [6, 52, 69, 75, 78] and photometric compensation [2, 19, 23, 37, 47, 74], full projector compensation can be achieved to rectify projections on non-planar and textured surfaces, ensuring optimal visual effects.

Although recent advancements in Convolutional Neural Network-based schemes [24, 26, 32, 33, 72, 73] have greatly improved the convenience and quality of projection mapping, these methods are usually limited to a specific viewpoint, making them incapable of direct applica-

tion to novel viewpoints. Neural fields-based method [14] utilize multilayer perceptrons (MLPs) [7, 64, 83] for projection mapping. Despite their capability for novel viewpoint ProCams applications, this method requires an additional co-located light and a dark room (i.e., assumes no ambient light). Moreover, it suffers from low computational and memory efficiency.

In this paper, we propose GS-ProCams for efficient view-agnostic projection mapping. In particular, we first utilize 2D Gaussians [27] as ProCams scene representation, since the original 2D Gaussians do not explicitly capture Bidirectional Reflectance Distribution Function (BRDF), we augment each Gaussian point in space with BRDF attributes. Then, we capture images of the target surface within the scene from multiple camera viewpoints while using a fixed projector to project various patterns onto it. Afterward, we employ structure-from-motion (SfM) [58, 63] to determine the poses and intrinsic parameters of the projector and the cameras. Subsequently, we jointly reconstruct the target surface and the projector’s response by differentiable physically-based rendering across each viewpoint. Finally, we apply this trained GS-ProCams model to various view-agnostic ProCams applications, such as projection mapping and projector compensation, as shown in Fig. 1. Comprehensive experiments on ProCams simulation and projector compensation show clear advantages of our GS-ProCams over previous methods.

In summary, our primary contributions include:

- We present GS-ProCams, the first Gaussian Splatting-based framework for projector-camera systems. It integrates 2D Gaussians and physically-based rendering to efficiently model the geometric and photometric mappings of ProCams.
- Compared to NeRF-based ProCams, GS-ProCams eliminates the need for additional devices, can operate under ambient room light, and is 600 times faster while using only 1/10 of the GPU memory.
- GS-ProCams can be applied to multiple view-agnostic ProCams applications simultaneously, including projection mapping and projector compensation.
- We introduce a view-agnostic ProCams benchmark encompassing various viewpoints, textured surfaces, and ambient lighting conditions for training and evaluating ProCams models. This benchmark is designed to foster future research in the field.

2. Related Work

2.1. ProCams simulation

ProCams simulation aims to model the real-world photometric and geometric mappings of projector-camera systems (ProCams) within a computational space. Once these mappings are established, the simulation synthesizes cam-

Table 1. **Comparison of representative schemes for ProCams and proposed GS-ProCams.** GS-ProCams is a view-agnostic method, which enables multi-view applications. It also simultaneously addresses geometric and photometric mappings under ambient light, using only an RGB camera and a projector.

Method	View-agnostic method	W/o manual calibration	W/o extra devices	Ambient light
LTM [74]	✗	✓	✓	✓
CNN-based [24]	✗	✗	✓	✓
Depth-prior DR [51]	✗	✓	✗	✗
NeRF-like DR [14]	✓	✓	✗	✗
GS-ProCams (Ours)	✓	✓	✓	✓

CNN: Convolutional Neural Network; DR: Differentiable Rendering

era images corresponding to various projections. ProCams simulation facilitates image-based relighting [14, 24, 74], shape reconstruction [24, 43, 60], and projector compensation [26, 32]. Early methods describe the pixel mapping from projectors to cameras using the Light Transport Matrix (LTM) [49, 50, 59, 74]. However, the reconstruction quality of LTM, which is based on the linear relationship between pixels, generally depends on dense sampling and specialized computational designs of large matrices [10, 11, 49, 59, 70, 74]. By employing neural rendering, DeProCams [24] generates photorealistic simulations of ProCams with fewer image samples by incorporating inherent epipolar geometric and simplified photometric constraints under a fixed viewpoint. However, a notable limitation of this approach is its reliance on manual calibration of ProCams using a checkerboard pattern [25], rather than leveraging data priors [58]. Although Park et al. [51] examine the geometric and photometric mappings in ProCams using a differentiable rendering scheme, it remains limited to specific view information and relies on an RGB-D camera. Additionally, the method depends heavily on pixel-level bias corrections. Erel et al. [14] integrate projectors into Neural Reflectance Fields [7, 64, 83] to enable view-agnostic projection mapping within 3D scenes. Despite this progress [14], the influence of other light sources within the scene is neglected, and a light source co-located with the camera is required, thereby causing limited applicability. We summarize the characteristics of technologies for ProCams simulation to provide an intuitive comparison with our approach in Tab. 1.

2.2. Projector compensation

Projector compensation aims to adjust projections for non-planar and textured surfaces to achieve the best visual display effect by optimizing the projector’s input patterns. Typically, projector compensation can be conducted separately through geometric correction [6, 52, 69, 75, 78] and radiometric compensation [2, 19, 23, 37, 47]. Upon completing the ProCams simulation, the compensated projec-

tion patterns can be obtained by multiplying the desired images with the inverse LTM [74]. Differentiable ProCams [14, 24, 51] generate projection patterns by making the synthesized scene closely approximate the desired images. On the other hand, comprehensive CNN-based architectures enable end-to-end projector compensation by ingeniously integrating geometric correction estimation represented by the warping grid [26, 72] or optical flow [33, 40, 73] with another component for photometric compensation. However, these methods are typically constrained to a specific viewpoint and smooth, uniform surfaces. Erel et al. [14] achieve projector compensation from novel viewpoints by integrating a projector into Neural Reflectance Fields [7, 64, 83]. Despite that, this method, which relies on ray-casting and MLPs, poses challenges to computational and memory resources. Additionally, this method assumes no ambient light in the scene.

2.3. Gaussian splatting and inverse rendering

3D Gaussian Splatting (3DGS) [35] has quickly sparked widespread interest due to its real-time differentiable rendering capability. While achieving rendering quality comparable to the state-of-the-art methods in novel view synthesis [4, 16, 42, 46, 77], it significantly enhances the efficiency of training and rendering. Furthermore, inverse rendering schemes extend 3DGS for materials and ambient lighting estimations [17, 31, 41].

While 3DGS [35] focuses primarily on efficient image rendering capabilities, reconstructing precise geometric shapes directly from Gaussian points poses significant challenges [9, 20, 27, 68, 80, 81]. In contrast, 2D Gaussian Splatting (2DGS) [27] uses 2D Gaussian primitives to ensure geometric consistency across multiple viewpoints. We enhance 2DGS with BRDF parameterization to capture the interactions between projector lighting and surfaces. We first use 2DGS to generate depth and materials maps in the camera frame and then perform shading calculations. The entire process is fully explicit and differentiable.

3. GS-ProCams

3.1. Preliminary

2DGS [27] employs explicit 2D Gaussians to represent scene geometry. The following primary components distinguish each 2D Gaussian point: its central point \mathbf{p}_k , two principal tangential vectors \mathbf{t}_u and \mathbf{t}_v , and a scaling vector $\mathbf{s} = (s_u, s_v)$ which regulates the variances of the 2D Gaussian distribution. Consequently, 2D Gaussians inherently include inherent normals defined by the above tangential vectors as $\mathbf{t}_w = \mathbf{t}_u \times \mathbf{t}_v$. In world space, every 2D Gaussian is defined in a local tangent plane and parameterized as:

$$P(u, v) = \mathbf{p}_k + s_u \mathbf{t}_u u + s_v \mathbf{t}_v v. \quad (1)$$

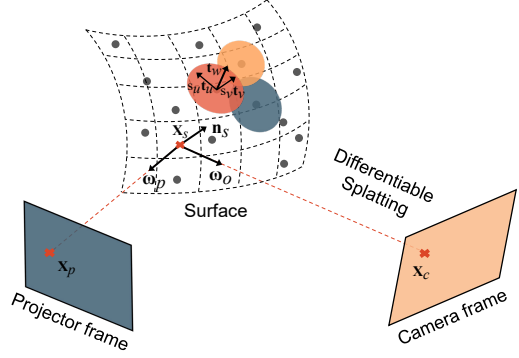


Figure 2. **GS-ProCams setup.** The intersection point \mathbf{x}_s of the ray from the camera and the target surface is determined by 2D Gaussians. The direct light from the projector illuminates this point.

Then, the 2D Gaussian value for a point $\mathbf{u} = (u, v)$ in its local space can be evaluated by the standard Gaussian:

$$G(\mathbf{u}) = \exp\left(-\frac{u^2 + v^2}{2}\right). \quad (2)$$

Additionally, each 2D Gaussian primitive possesses an opacity o and a view-dependent appearance \mathbf{c} represented using spherical harmonics (SH). Finally, given the viewpoint-based color \mathbf{c}_i of each Gaussian point, the pixel color \mathbf{C} is obtained through alpha blending with K tile-based Gaussians arranged according to the depth values of their center locations:

$$\mathbf{C}(\mathbf{x}) = \sum_{i \in K} W_i \mathbf{c}_i, \quad W_i = \alpha_i \prod_{j=1}^{i-1} (1 - \alpha_j), \quad (3)$$

where $\alpha = o \cdot \hat{G}(u(\mathbf{x}))$. Here, $\hat{G}(u(\mathbf{x}))$ is the result of applying a low-pass filter to $G(u(\mathbf{x}))$, and \mathbf{x} denotes a homogeneous ray that originates from the camera and traverses the UV space.

The orientation of a 2D Gaussian can be construed as a rotation matrix $\mathbf{R} = [\mathbf{t}_u, \mathbf{t}_v, \mathbf{t}_w]$ and be represented in the form of a unit quaternion \mathbf{q} during optimization. In summary, each 2D Gaussian is parameterized by several learnable parameters as $\{\mathbf{p}, \mathbf{q}, \mathbf{s}, o, \mathbf{c}\}$. Furthermore, the designed density control mechanism enables adaptive regulation of the total number of points and the density within a unit volume.

3.2. ProCams modeling

The core of our proposed GS-ProCams is establishing the geometric and photometric mappings of projector-camera systems (ProCams) using Gaussian splatting, thus achieving high-fidelity ProCams simulation. Consider a point \mathbf{x}_s on the target surface within a scene, which is captured by the camera as \mathbf{x}_c in the camera frame, as illustrated in Fig. 2. In

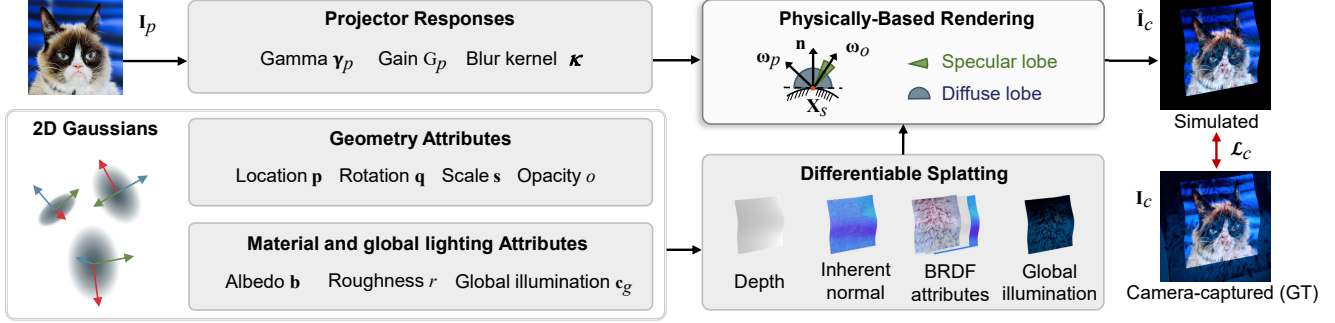


Figure 3. **Pipeline.** GS-ProCams uses 2D Gaussians to represent the scene, then obtains the geometry and materials of the target surface, as well as the global illumination component, through differentiable splatting techniques [27]. By using various projection patterns and capturing images from different viewpoints, GS-ProCams jointly optimizes the explicit projector responses and attributes of the 2D Gaussian points listed on the left through physically-based differentiable rendering.

the absence of occlusion, this point is illuminated by \mathbf{x}_p in the projector frame. Furthermore, \mathbf{x}_s is affected by ambient and complex indirect lighting, i.e., global illumination. Taking these factors into consideration, We utilize the classical rendering equation [34] to describe the relationship between outgoing and incoming light at point \mathbf{x}_s as follows:

$$L_o(\omega_o, \mathbf{x}_s) = \int_{\Omega} f(\omega_o, \omega_i, \mathbf{x}_s) L_i(\omega_i, \mathbf{x}_s) (\omega_i \cdot \mathbf{n}_s) d\omega_i, \quad (4)$$

where Ω represents the upper hemisphere centered at \mathbf{x}_s , with the normal vector \mathbf{n}_s and f denotes the BRDF. We employ 2D Gaussians described in 2D Gaussian Splatting (2DGS) [27] as foundational primitives, extending their original attributes by BRDF parameterization to capture the interactions between the light and the target surface. Building upon this, We capture a series of images of the surface $\{\mathbf{I}_c^m\}_{m=1}^M$ from multiple viewpoints, which is illuminated by known projector input patterns $\{\mathbf{I}_p^n\}_{n=1}^N$. Then, we simultaneously estimate the surface’s unknown geometric and material properties utilizing physically-based rendering (PBR). We illustrate the pipeline of our proposed GS-ProCams in Fig. 3.

3.3. Attributes from Gaussians

As shown in Fig. 3, we first derive attributes of the target surface from 2D Gaussians. The attributes can generally be divided into three categories: (1) the depth and inherent normals from geometry attributes of Gaussians; (2) the BRDF attributes for material reflectance; and (3) the global illumination component, approximated by RGB residuals. Notably, we utilize normals derived from depth gradients in the shading computations, while use inherent normals to regularize geometric consistency.

Depth. The intersections between camera rays and the surface are determined by their depths in the camera frame. We use the same approach as 2DGS [27] and render the mean

depth D by Eq. (3) to represent the ray-surface intersection as follows:

$$D = \sum_{i \in K} \frac{W_i z_i}{\sum_{i \in K} W_i}, \quad (5)$$

where \mathbf{x} is the homogeneous ray corresponding to the camera pixel $\mathbf{x}_c = (x, y)$, and z_i denotes the depth of the intersection between \mathbf{x} and the i -th Gaussian planes.

Normal. To enhance depth consistency and surface smoothness, we utilize normals derived from viewpoint depth rather than the inherent normals aligned with the directions of their highest density gradients as the normal map \mathbf{N} :

$$\mathbf{N}(x, y) = \frac{\nabla_x \mathbf{d} \times \nabla_y \mathbf{d}}{|\nabla_x \mathbf{d} \times \nabla_y \mathbf{d}|}, \quad (6)$$

where x and y denote the coordinates of the pixel \mathbf{x}_c in the depth map D .

BRDF attributes. To enable the light-surface interactions, we augment each original 2D Gaussian point [27] with additional learnable attributes: albedo $\mathbf{b} \in [0, 1]^3$ and roughness $r \in [0, 1]$. Then we splat these attributes onto the camera frame by utilizing the efficient differentiable rasterization method described by Eq. (3):

$$\{\mathbf{B}, R\} = \sum_{i \in K} W_i \{\mathbf{b}_i, r_i\}, \quad (7)$$

where \mathbf{B} and R represent the maps of albedo and roughness after rasterization in a specified viewpoint.

3.4. Lighting

In ProCams settings, light usually comes from the environment and the projector. The projector pixels act like high-power spotlight light sources that dominate the light contribution. Therefore, we model the incident light at \mathbf{x}_s as the sum of projector direct light, denoted as L_p , and the global illumination, denoted as L_g .

Projector direct light. Denote the projector gamma as γ_p , which converts standard sRGB color into linear RGB space. Denote the projector’s luminous power as G_p , and assume constant light attenuation. Additionally, due to the projector’s optical characteristics, e.g., point spread function (PSF) [38], the projected light suffers from defocus. Therefore, we use a learnable 5×5 kernel κ to model the projector’s PSF. Consequently, the projector emitted direct light L_p can be expressed as:

$$L_p(\mathbf{x}_s) = \kappa * (G_p \cdot \mathbf{I}_p^{\gamma_p}(\mathbf{x}_p)), \quad (8)$$

where \mathbf{x}_p is the projector pixel that directly illuminates the surface point \mathbf{x}_s , as shown in Fig. 2, and $*$ is the convolution operator. Denote the projector projection matrix as \mathbf{M}_p , the relationship between \mathbf{x}_p and \mathbf{x}_s is given by

$$\bar{\mathbf{x}}_p = \mathbf{M}_p \bar{\mathbf{x}}_s, \quad (9)$$

where $\bar{\mathbf{x}}_p$ and $\bar{\mathbf{x}}_s$ denote the homogeneous coordinates of \mathbf{x}_p and \mathbf{x}_s , respectively. Then, according to Eq. (4), the outgoing/reflected direct light at \mathbf{x}_s can be computed by:

$$\mathbf{C}_p(\omega_o, \mathbf{x}_s) = f(\omega_o, \omega_p, \mathbf{x}_s) L_p(\omega_p, \mathbf{x}_s) (\omega_p \cdot \mathbf{n}_s), \quad (10)$$

where the normal \mathbf{n}_s of the surface point \mathbf{x}_s is determined by Eq. (6). We approximate the BRDF f in Eq. (10) using a simplified Disney BRDF model [8].

Global illumination. In most ProCams settings, projector direct light dominates the illumination, therefore, we utilize a simplified generalized estimate to replace the precise yet complex calculations for efficiency. Inspired by 3DGS [35] and 2DGS [27], we approximate the global illumination radiance as a view-dependent color $\mathbf{c}_r(\omega_o)$ by maintaining a set of coefficients of the spherical harmonics for each Gaussian point and then rasterize the color using alpha blending according to Eq. (3) as follows:

$$\mathbf{C}_g = \sum_{i \in K} W_i \mathbf{c}_{g_i}. \quad (11)$$

Finally, the camera-captured color is given by

$$\hat{\mathbf{I}}_c = \text{clamp} \left((\mathbf{C}_p + \mathbf{C}_g)^{\frac{1}{\gamma_c}}, 0, 1 \right), \quad (12)$$

where γ_c is a gamma tone mapping function [1].

3.5. Optimization

As shown in Fig. 3, the optimizable parameters associated with each Gaussian point are $\{\mathbf{p}, \mathbf{q}, \mathbf{s}, o, \mathbf{c}_g, \mathbf{b}, r\}$. The optimizable parameters of projector responses are $\{\gamma_p, G_p, \kappa\}$. We impose the following constraints to optimize the GS-ProCams parameters.

Photometric loss. In line with 3DGS [35], we consider the combined loss function of \mathcal{L}_1 and D-SSIM \mathcal{L}_{D-SSIM} to

minimize the photometric difference between the simulated result $\hat{\mathbf{I}}_c$ and camera captured ground truth \mathbf{I}_c and set the weight $\lambda = 0.2$:

$$\mathcal{L}_c = (1 - \lambda) \mathcal{L}_1 + \lambda \mathcal{L}_{D-SSIM}. \quad (13)$$

Geometric regularization. We also employ depth distortion loss and normal consistency loss [27] to encourage the 2D primitives to align with the thin surfaces closely:

$$\mathcal{L}_d = \sum_{i,j} w_i w_j |z_i - z_j|, \quad \mathcal{L}_n = \sum_i w_i (1 - \mathbf{n}_i^\top \mathbf{N}), \quad (14)$$

where \mathbf{n}_i is the inherent normal of the the intersection between \mathbf{x} and the i -th splat.

Materials regularization. In this paper, we estimate surface materials from realistic scenes where roughness maps are anticipated to exhibit smooth characteristics in regions with uniform color [79]. Consequently, we define a bilateral smoothness term, guided by the albedo, as follows:

$$\mathcal{L}_{material} = \|\nabla R\| \exp(-\|\nabla \mathbf{B}\|). \quad (15)$$

Note that we detach the gradient propagation of the albedo \mathbf{B} before computing this loss.

Mask entropy. Most projector applications focus only on regions of interest, such as the projector’s FOV [26] or objects [14], typically using binary masks to indicate these areas. In light of this, We introduce a cross-entropy constraint [71] to regularize the optimization for obtaining opaque surfaces by forcing the accumulated opacity $O = \sum_{i \in K} W_i$ to be aligned with the mask O_m . The constraint is defined as:

$$\mathcal{L}_{entropy} = -O_m \log O - (1 - O_m) \log(1 - O), \quad (16)$$

Total Loss. Finally, we train GS-ProCams with the following loss function:

$$\mathcal{L} = \mathcal{L}_c + \lambda_d \mathcal{L}_d + \lambda_n \mathcal{L}_n + \lambda_m \mathcal{L}_{material} + \lambda_e \mathcal{L}_{entropy}, \quad (17)$$

where λ_d , λ_n , λ_m , and λ_e represent the weights for the respective loss terms, which are set to 1000, 0.05, 0.002 and 0.1, respectively. We jointly optimize the GS-ProCams parameters using Adam optimizer [36] for 30,000 training steps.

4. Experiments

To demonstrate the advantages of our approach, we compared it with several state-of-the-art ProCams simulation and/or projector compensation methods [14, 24, 26] in Sec. 4.1 and Sec. 4.2. In our experiments, we employed Peak Signal-to-Noise Ratio (PSNR), Structural Similarity Index Measure (SSIM), and Learned Perceptual Image

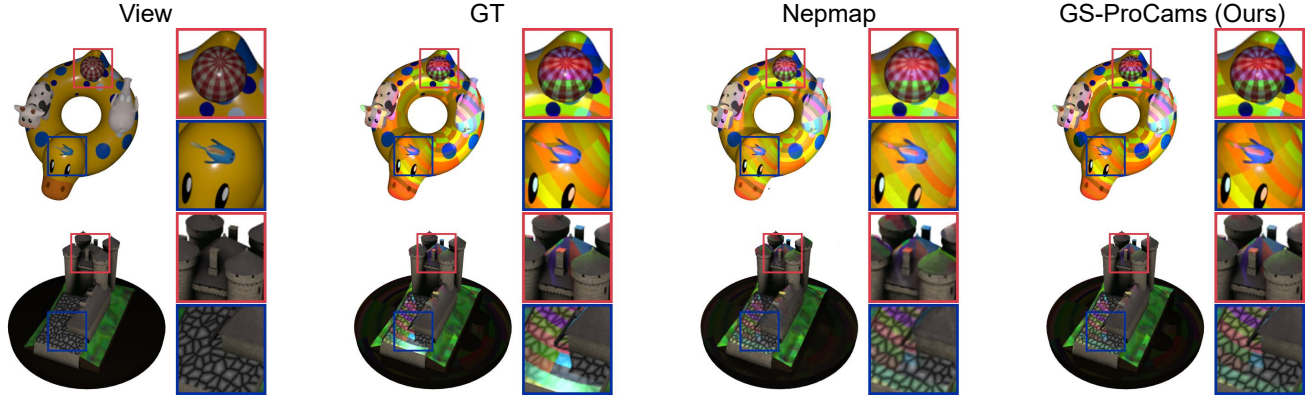


Figure 4. **Visual comparisons of ProCams simulation on the Nepmap synthetic dataset [14].** The first column displays an object from a novel viewpoint, the second column shows the object under a novel projection pattern, and the third and fourth columns present the results of two methods. We present two of the four scenes here as examples. Compared to Nepmap, our model exhibits finer details and more realistic color. Moreover, our method outperforms Nepmap on computation and memory efficiency by a significant margin (Table 2). See supplementary material for more results.

Table 2. **ProCams simulation results on the Nepmap synthetic dataset [14].** Results are averaged over 4 different scenes.

Method	PSNR \uparrow	SSIM \uparrow	LPIPS \downarrow	Time	FPS	Memory
Nepmap [14]	27.23	0.945	0.061	> 3hrs	0.36	34.88 GB
GS-ProCams	33.07	0.974	0.032	9.3 min	222	2.02 GB

Patch Similarity (LPIPS) [82] to evaluate the ProCams simulation, and projector compensation quality. Additionally, we statistically examined the memory requirements, training time, and inference frames per second (FPS) on an NVIDIA A800 GPU.

4.1. Synthetic dataset

We compared our GS-ProCams with the state-of-the-art NeRF-based ProCams simulation approach [14], using their synthetic dataset to evaluate the ProCams simulation quality. We refer to this method as *Nepmap* for convenience. We utilized the four synthetic scenes released by Nepmap and their pre-trained models to compare 36 novel viewpoints and novel projection patterns for each scene. Quantitative results are presented in Tab. 2, and qualitative comparisons are illustrated in Fig. 4. The results indicate that our model not only outperforms Nepmap in terms of quality but also shows a significant improvement in efficiency, *i.e.*, about 600 times faster and only uses 1/10 of GPU memory. Furthermore, our model does not require additional devices and takes ambient light into account as listed in Tab. 1.

4.2. Real-world benchmark dataset

We collected a benchmark dataset in real indoor lighting environments. Our projector-camera system consists of a Panasonic Lumix DC-S5 camera and an EPSON CB-965

projector, and an RGB fill light was employed to create various ambient lighting conditions. It is worth noting that unlike Nepmap [14], our method does not require additional light sources to work, the RGB fill light is only used to change ambient lighting conditions. The projector and camera resolutions are both set to 800×800 .

We projected multiple patterns for each viewpoint, including a fixed pattern to enhance surface texture for the SfM process [58] and a natural image for model training. We followed the methodology outlined in [26] to obtain projector FOV masks. In our experimental configuration, we projected natural patterns across 48 viewpoints. At the 48th viewpoint, an additional 48 natural patterns were projected for validation. Subsequently, we randomly repositioned the camera and projected 48 patterns once more to evaluate the applicability of our method from this novel viewpoint. See supplementary material for more details.

Because Nepmap [14] requires a light source to be co-located with the camera and only works for a dark room, we cannot compare with it on our ProCams settings. Instead, we compare with two state-of-the-art view-specific methods [24, 26].

ProCams simulation. We use the state-of-the-art method, *DeProCams* [24] (view-specific), as a baseline to evaluate the effectiveness of our approach (view-agnostic) at the unseen novel viewpoint. We present quantitative comparisons in Tab. 3 and illustrate qualitative findings with a scene example in Fig. 5. For the trained viewpoint, our GS-ProCams outperforms DeProCams, due to our GS-based formulation. For the unseen novel viewpoint, DeProCams shows better simulation quality, because it is view-specific and is trained on this viewpoint, while our GS-ProCams has never seen this viewpoint. Our method highlights its advantages com-

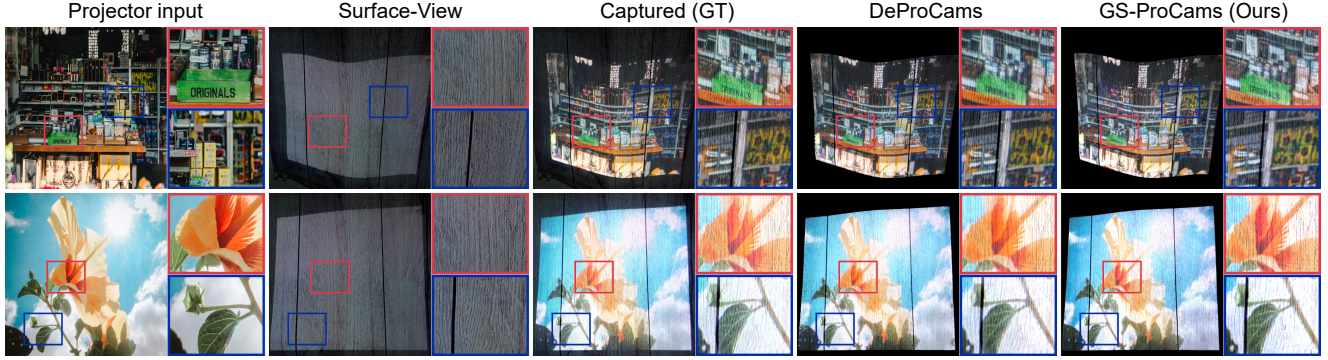


Figure 5. **Visual comparisons of ProCams simulation on real-world benchmark dataset.** We compare with DeProCams [24] (view-specific) at the last training viewpoint (first row) and at the novel viewpoint that our GS-ProCams has not previously seen (second row). Note that DeProCams (view-specific) necessitates repeated data acquisition and training for the novel viewpoint, whereas our approach can generalize to novel viewpoints. The first column displays the projector input pattern, the second column shows the surface (no superimposed projection) from the viewpoint, and the subsequent columns sequentially illustrate the camera-captured ground truth and the simulations results. See supplementary material for more results.

Table 3. **ProCams simulation comparisons on real-world benchmark dataset.** Results are averaged over 10 different scenes. Note that DeProCams needs to additionally capture training data and retraining for novel viewpoints, while our GS-ProCams waives this requirement.

Method	Trained Viewpoint				Unseen Novel Viewpoint				
	PSNR \uparrow	SSIM \uparrow	LPIPS \downarrow	Training Time	PSNR \uparrow	SSIM \uparrow	LPIPS \downarrow	Training Time	GPU Memory
DeProCams ¹ [24]	28.66	0.907	0.109	4.61 min	27.63	0.886	0.134	4.62 min	26.73 GB
w/o PSF (Ours) ²	25.76	0.887	0.104	15.86 min	24.83	0.837	0.121	0	3.38 GB
GS-ProCams (Ours) ²	27.22	0.911	0.083	15.69 min	26.11	0.859	0.100	0	3.49 GB

¹ View-specific method; ² View-agnostic method

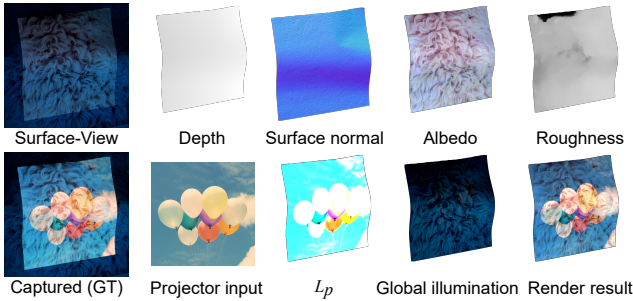


Figure 6. **Intermediate results.** GS-ProCams uses interpretable parameters to establish the geometric and photometric mappings of ProCams, jointly estimating them while achieving view-agnostic ProCams simulation. Here, “ L_p ” is in the linear color space. “Albedo” and “Global illumination” are converted from linear to sRGB color space for better visual experience.

pared to the view-specific approach. First, our method facilitates the synthesis of surface appearances with novel projections under novel viewpoints. Second, our method demonstrates a significant efficiency advantage in memory usage. Additionally, as previously noted, GS-ProCams effectively solves the view-agnostic projection mapping prob-

lem by physically-based rendering, while deriving interpretable quantities from multi-view images as shown in Fig. 6.

Projector compensation. Our proposed method facilitates ProCams simulation through a fully differentiable process, enabling the optimization of projection patterns to align rendered images with the desired effects. Once trained, our method allows for direct projector compensation from novel viewpoints without retraining or fine-tuning. We compare with two state-of-the-art projector compensation methods *CompenNeSt++* [26] (view-specific) and *DeProCams* [24] (view-specific). The quantitative results are summarized in Tab. 4, while the visual comparisons are illustrated in Fig. 7. The results show that our method outperforms DeProCams under the trained viewpoint and is comparable to *CompenNeSt++*. For the novel viewpoint, there is a gap between our model and *CompenNeSt++*, but it still outperforms DeProCams. This is because both *CompenNeSt++* and DeProCams are retrained for the novel viewpoint, but our GS-ProCams is directly applied to the novel viewpoint without retraining. The view-agnostic projector compensation and low memory requirements demonstrate our significant advantages in practical applications.

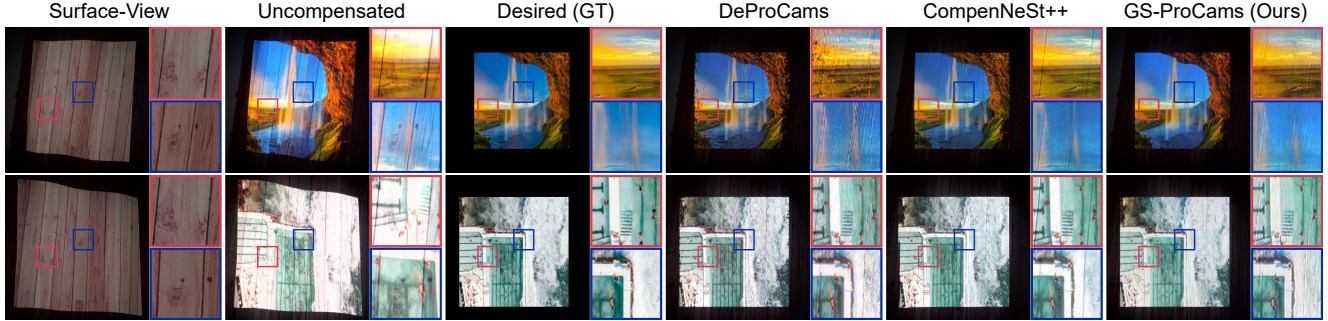


Figure 7. **Visual comparisons of projector compensation on real-world benchmark dataset.** Similar to ProCams simulation (Fig. 5), the camera-captured results from different viewpoints within the scene are presented in two rows. Our model is applied directly to novel viewpoints without retraining in the second row, while the other two view-specific methods necessitate repeated data capturing and training. The first three columns respectively illustrate the surface appearance from the specified viewpoint, the uncompensated appearance, and the expected appearance. The last three columns display the compensated results from different models. Note that our method effectively compensates for geometry and photometry when applied to the novel viewpoint. See supplementary material for more results.

Table 4. **Projector compensation results on real-world dataset.** Results are averaged over 10 different scenes. Our approach is directly applied to the unseen novel viewpoint without retraining, while the other two methods must be retrained.

Method	Trained Viewpoint				Unseen Novel Viewpoint				
	PSNR \uparrow	SSIM \uparrow	LPIPS \downarrow	Training Time	PSNR \uparrow	SSIM \uparrow	LPIPS \downarrow	Training Time	GPU Memory
DeProCams ¹ [24]	22.78	0.816	0.189	4.61 min	22.35	0.796	0.217	4.62 min	26.73 GB
CompenNeSt++ ¹ [26]	24.02	0.834	0.161	13.25 min	24.05	0.830	0.173	13.21 min	30.79 GB
GS-ProCams (Ours) ²	23.91	0.828	0.173	15.69 min	23.66	0.807	0.194	0	3.49 GB
Uncompensated	14.80	0.669	0.281	-	14.57	0.641	0.303	-	-

¹ View-specific method; ² View-agnostic method

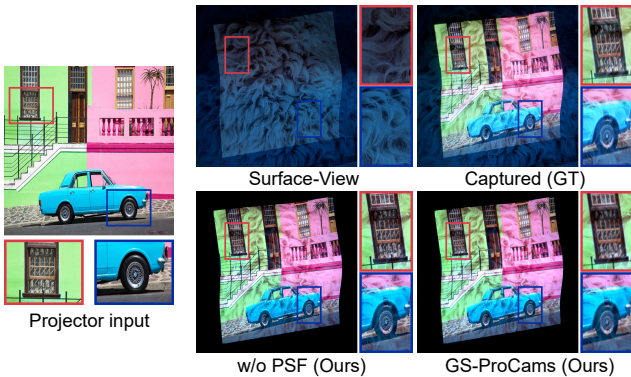


Figure 8. **Ablation study of PSF estimation.** We compare GS-ProCams with a degraded version that ignores projector PSF. Note that the result of “w/o PSF” shown in the zoomed-in patches exhibits unrealistically sharp projections.

4.3. Ablation study

We conducted ablation study on the real-world benchmark dataset to validate the effectiveness of the projector’s PSF estimation (Eq. (8)). We denote GS-ProCams without PSF as *w/o PSF*. The quantitative and qualitative results are

shown in Tab. 3 and Fig. 8, respectively. Clearly, without estimating the projector’s PSF, the synthesized results ignores projector defocus, and exhibit unrealistically sharp projections, while GS-ProCams results are much closer to the camera-captured ground truth.

5. Conclusion

We introduce GS-ProCams, the first Gaussian Splatting-based framework for projector-camera systems (ProCams). This framework enables efficient novel viewpoint ProCams simulation and projector compensation without retraining. Compared with NeRF-based ProCams, our GS-ProCams waives the need for additional devices, and achieves higher ProCams simulation quality. Moreover, it is 600 times faster and uses only 1/10 of the GPU memory.

Limitations and future work. GS-ProCams has limitations in regions with strong specular reflections. More intricate photometric mapping calculations and optimization strategies are expected to further improve the framework’s performance, how to balance the simulation quality and efficiency is worth exploring in future work.

References

- [1] Matthew Anderson, Ricardo Motta, Srinivasan Chandrasekar, and Michael Stokes. Proposal for a standard default color space for the internet—srgb. In *Color and imaging conference*, pages 238–245. Society of Imaging Science and Technology, 1996. 5
- [2] M. Ashdown, T. Okabe, I. Sato, and Y. Sato. Robust content-dependent photometric projector compensation. In *CVPRW*, pages 6–6, 2006. 1, 2
- [3] Seyed Ehsan Marjani Bajestani and Giovanni Beltrame. Event-based rgb sensing with structured light. In *WACV*, pages 5458–5467, 2023. 1
- [4] Jonathan T. Barron, Ben Mildenhall, Dor Verbin, Pratul P. Srinivasan, and Peter Hedman. Mip-nerf 360: Unbounded anti-aliased neural radiance fields. In *CVPR*, pages 5470–5479, 2022. 3
- [5] Luca Bartolomei, Matteo Poggi, Fabio Tosi, Andrea Conti, and Stefano Mattoccia. Active stereo without pattern projector. In *ICCV*, pages 18470–18482, 2023. 1
- [6] Ameneh Boroomand, Hicham Sekkati, Mark Lamm, David A. Clausi, and Alexander Wong. Saliency-guided projection geometric correction using a projector-camera system. In *ICIP*, pages 2951–2955, 2016. 1, 2
- [7] Mark Boss, Varun Jampani, Raphael Braun, Ce Liu, Jonathan Barron, and Hendrik PA Lensch. Neural-pil: Neural pre-integrated lighting for reflectance decomposition. In *NeurIPS*, pages 10691–10704. Curran Associates, Inc., 2021. 2, 3
- [8] Brent Burley and Walt Disney Animation Studios. Physically-based shading at disney. In *Acm Siggraph*, pages 1–7. vol. 2012, 2012. 5, 1
- [9] Hanlin Chen, Chen Li, and Gim Hee Lee. Neusg: Neural implicit surface reconstruction with 3d gaussian splatting guidance. *arXiv preprint arXiv:2312.00846*, 2023. 3
- [10] Paul Debevec, Tim Hawkins, Chris Tchou, Haarm-Pieter Duiker, Westley Sarokin, and Mark Sagar. Acquiring the reflectance field of a human face. In *SIGGRAPH*, pages 145–156, 2000. 2
- [11] Paul E. Debevec, Tim Hawkins, Chris Tchou, Haarm-Pieter Duiker, Westley Sarokin, and Mark Sagar. Acquiring the reflectance field of a human face. *Seminal Graphics Papers: Pushing the Boundaries, Volume 2*, 2000. 2
- [12] Ashish Doshi, Ross T Smith, Bruce H Thomas, and Con Bouras. Use of projector based augmented reality to improve manual spot-welding precision and accuracy for automotive manufacturing. *The International Journal of Advanced Manufacturing Technology*, 89:1279–1293, 2017. 1
- [13] Tinglin Duan, Parinya Punpongsanon, Daisuke Iwai, and Kosuke Sato. Flyinghand: extending the range of haptic feedback on virtual hand using drone-based object recognition. In *SIGGRAPH Asia 2018 Technical Briefs*, New York, NY, USA, 2018. ACM.
- [14] Yotam Erel, Daisuke Iwai, and Amit H. Bermano. Neural projection mapping using reflectance fields. *IEEE TVCG*, 29:4339–4349, 2023. 2, 3, 5, 6
- [15] Yotam Erel, Or Kozlovsky-Mordenfeld, Daisuke Iwai, Kosuke Sato, and Amit H. Bermano. Casper dpm: Cascaded perceptual dynamic projection mapping onto hands. In *SIGGRAPH Asia*, New York, NY, USA, 2024. Association for Computing Machinery. 1
- [16] Sara Fridovich-Keil, Alex Yu, Matthew Tancik, Qinhong Chen, Benjamin Recht, and Angjoo Kanazawa. Plenoxels: Radiance fields without neural networks. In *CVPR*, pages 5501–5510, 2022. 3
- [17] Jian Gao, Chun Gu, Youtian Lin, Zhihao Li, Hao Zhu, Xun Cao, Li Zhang, and Yao Yao. Relightable 3d gaussians: Realistic point cloud relighting with brdf decomposition and ray tracing. In *ECCV*, pages 73–89, Cham, 2025. Springer Nature Switzerland. 3
- [18] Jason Geng. Structured-light 3d surface imaging: a tutorial. *Adv. Opt. Photon.*, 3(2):128–160, 2011. 1
- [19] Anselm Grundhöfer and Daisuke Iwai. Robust, error-tolerant photometric projector compensation. *IEEE Transactions on Image Processing*, 24(12):5086–5099, 2015. 1, 2
- [20] Antoine Guédon and Vincent Lepetit. Sugar: Surface-aligned gaussian splatting for efficient 3d mesh reconstruction and high-quality mesh rendering. In *CVPR*, pages 5354–5363, 2024. 3
- [21] Roy Hachnochi, Mingrui Zhao, Nadav Orzech, Rinon Gal, Ali Mahdavi-Amiri, Daniel Cohen-Or, and Amit Haim Bermano. Cross-domain compositing with pretrained diffusion models. *arXiv preprint arXiv:2302.10167*, 2023. 1
- [22] Jeremy Hartmann, Yen-Ting Yeh, and Daniel Vogel. Aar: Augmenting a wearable augmented reality display with an actuated head-mounted projector. In *UIST*, page 445–458, New York, NY, USA, 2020. ACM. 1
- [23] Bingyao Huang and Haibin Ling. End-to-end projector photometric compensation. In *CVPR*, 2019. 1, 2
- [24] Bingyao Huang and Haibin Ling. Deprocams: Simultaneous relighting, compensation and shape reconstruction for projector-camera systems. *IEEE TVCG*, 27(5):2725–2735, 2021. 1, 2, 3, 5, 6, 7, 8
- [25] Bingyao Huang, Ying Tang, Samed Ozdemir, and Haibin Ling. A fast and flexible projector-camera calibration system. *IEEE Transactions on Automation Science and Engineering*, 18(3):1049–1063, 2021. 2
- [26] Bingyao Huang, Tao Sun, and Haibin Ling. End-to-end full projector compensation. *TPAMI*, 44(6):2953–2967, 2022. 1, 2, 3, 5, 6, 7, 8
- [27] Binbin Huang, Zehao Yu, Anpei Chen, Andreas Geiger, and Shenghua Gao. 2d gaussian splatting for geometrically accurate radiance fields. In *SIGGRAPH*, New York, NY, USA, 2024. ACM. 2, 3, 4, 5
- [28] Daisuke Iwai. Projection mapping technologies: A review of current trends and future directions. *Proceedings of the Japan Academy, Series B*, 100(3):234–251, 2024. 1
- [29] D. Iwai, S. Hanatani, C. Horii, and K. Sato. Limpid desk: Transparentizing documents on real desk in projection-based mixed reality. In *IEEE VR*, pages 319–319, 2006. 1
- [30] Daisuke Iwai, Ryo Matsukage, Sota Aoyama, Tsuyoshi Kikukawa, and Kosuke Sato. Geometrically consistent projection-based tabletop sharing for remote collaboration. *IEEE Access*, 6:6293–6302, 2018. 1

- [31] Yingwenqi Jiang, Jiadong Tu, Yuan Liu, Xifeng Gao, Xiaoxiao Long, Wenping Wang, and Yuexin Ma. Gaussianshader: 3d gaussian splatting with shading functions for reflective surfaces. In *CVPR*, pages 5322–5332, 2024. 3
- [32] Yuta Kageyama, Daisuke Iwai, and Kosuke Sato. Online projector deblurring using a convolutional neural network. *IEEE TVCG*, 28(5):2223–2233, 2022. 1, 2
- [33] Yuta Kageyama, Daisuke Iwai, and Kosuke Sato. Efficient distortion-free neural projector deblurring in dynamic projection mapping. *IEEE TVCG*, pages 1–14, 2024. 1, 3
- [34] James T. Kajiya. The rendering equation. *SIGGRAPH Comput. Graph.*, 20(4):143–150, 1986. 4
- [35] Bernhard Kerbl, Georgios Kopanas, Thomas Leimkuehler, and George Drettakis. 3d gaussian splatting for real-time radiance field rendering. *ACM Trans. Graph.*, 42(4), 2023. 3, 5
- [36] Diederik P. Kingma and Jimmy Ba. Adam: A method for stochastic optimization. In *ICLR*, 2015. 5
- [37] Philipp Kurth, Vanessa Lange, Marc Stamminger, and Frank Bauer. Real-time adaptive color correction in dynamic projection mapping. In *IEEE ISMAR*, pages 174–184, 2020. 1, 2
- [38] Hiroki Kusuyama, Yuta Kageyama, Daisuke Iwai, and Kosuke Sato. A multi-aperture coaxial projector balancing shadow suppression and deblurring. *IEEE TVCG*, pages 1–11, 2024. 5
- [39] Chunyu Li, Yusuke Monno, Hironori Hidaka, and Masatoshi Okutomi. Pro-cam ssm: Projector-camera system for structure and spectral reflectance from motion. In *ICCV*, pages 2414–2423, 2019. 1
- [40] Yuqi Li, Wenting Yin, Jiabao Li, and Xijiong Xie. Physics-based efficient full projector compensation using only natural images. *IEEE TVCG*, 30(8):4968–4982, 2024. 3
- [41] Zhihao Liang, Qi Zhang, Ying Feng, Ying Shan, and Kui Jia. Gs-ir: 3d gaussian splatting for inverse rendering. In *CVPR*, pages 21644–21653, 2024. 3
- [42] Ben Mildenhall, Pratul P. Srinivasan, Matthew Tancik, Jonathan T. Barron, Ravi Ramamoorthi, and Ren Ng. Nerf: representing scenes as neural radiance fields for view synthesis. *Commun. ACM*, 65(1):99–106, 2021. 3
- [43] Parsa Mirdehghan, Maxx Wu, Wenzheng Chen, David B Lindell, and Kiriakos N Kutulakos. Turbosl: Dense accurate and fast 3d by neural inverse structured light. In *CVPR*, pages 25067–25076, 2024. 1, 2
- [44] Wieland Morgenstern, Niklas Gard, Simon Baumann, Anna Hilsmann, and Peter Eisert. X-maps: Direct depth lookup for event-based structured light systems. In *CVPR*, pages 4007–4015, 2023. 1
- [45] Shohei Mori, Sei Ikeda, and Hideo Saito. A survey of diminished reality: Techniques for visually concealing, eliminating, and seeing through real objects. *IPSJ Transactions on Computer Vision and Applications*, 9:1–14, 2017. 1
- [46] Thomas Müller, Alex Evans, Christoph Schied, and Alexander Keller. Instant neural graphics primitives with a multiresolution hash encoding. *ACM Trans. Graph.*, 41(4), 2022. 3
- [47] Shree K Nayar, Harish Peri, Michael D Grossberg, and Peter N Belhumeur. A projection system with radiometric compensation for screen imperfections. In *ICCV workshop on projector-camera systems (PROCAMS)*, 2003. 1, 2
- [48] Hiroto Nishino, Etsuro Hatano, Satoru Seo, Takashi Nitta, Tomoyuki Saito, Masaaki Nakamura, Kayo Hattori, Muneo Takatani, Hiroaki Fuji, Kojiro Taura, et al. Real-time navigation for liver surgery using projection mapping with indocyanine green fluorescence: development of the novel medical imaging projection system. *Annals of surgery*, 267(6):1134–1140, 2018. 1
- [49] Matthew O’Toole and Kiriakos N. Kutulakos. Optical computing for fast light transport analysis. *ACM Trans. Graph.*, 29(6), 2010. 2
- [50] Matthew O’Toole, John Mather, and Kiriakos N. Kutulakos. 3d shape and indirect appearance by structured light transport. In *CVPR*, 2014. 2
- [51] Jino Park, Donghyuk Jung, and Bochang Moon. Projector compensation framework using differentiable rendering. *IEEE Access*, 10:44461–44470, 2022. 2, 3
- [52] R. Raskar. Immersive planar display using roughly aligned projectors. In *Proceedings IEEE Virtual Reality 2000 (Cat. No.00CB37048)*, pages 109–115, 2000. 1, 2
- [53] Robin Rombach, Andreas Blattmann, Dominik Lorenz, Patrick Esser, and Björn Ommer. High-resolution image synthesis with latent diffusion models. In *CVPR*, pages 10684–10695, 2022. 1
- [54] Joaquim Salvi, Sergio Fernandez, Tomislav Pribanic, and Xavier Llado. A state of the art in structured light patterns for surface profilometry. *Pattern recognition*, 43(8):2666–2680, 2010. 1
- [55] Giovanna Sansoni, Marco Trebeschi, and Franco Docchio. State-of-the-art and applications of 3d imaging sensors in industry, cultural heritage, medicine, and criminal investigation. *Sensors*, 9(1):568–601, 2009. 1
- [56] Yushi Sato, Daisuke Iwai, and Kosuke Sato. Responsive-extendedhand: Adaptive visuo-haptic feedback recognizing object property with rgb-d camera for projected extended hand. *IEEE Access*, 12:38247–38257, 2024. 1
- [57] Susanne Schmidt, Gerd Bruder, and Frank Steinicke. Effects of virtual agent and object representation on experiencing exhibited artifacts. *Computers & Graphics*, 83:1–10, 2019. 1
- [58] Johannes Lutz Schönberger and Jan-Michael Frahm. Structure-from-motion revisited. In *CVPR*, 2016. 2, 6, 1
- [59] Pradeep Sen, Billy Chen, Gaurav Garg, Stephen R. Marschner, Mark Horowitz, Marc Levoy, and Hendrik P. A. Lensch. Dual photography. In *SIGGRAPH*, page 745–755, New York, NY, USA, 2005. ACM. 2
- [60] Aarrushi Shandilya, Benjamin Attal, Christian Richardt, James Tompkin, and Matthew O’toole. Neural fields for structured lighting. In *ICCV*, pages 3512–3522, 2023. 1, 2
- [61] Suhyun Shin, Seokjun Choi, Felix Heide, and Seung-Hwan Baek. Dispersed structured light for hyperspectral 3d imaging. In *CVPR*, pages 24997–25006, 2024. 1
- [62] Christian Siegl, Vanessa Lange, Marc Stamminger, Frank Bauer, and Justus Thies. Faceforge: Markerless non-rigid face multi-projection mapping. *IEEE TVCG*, 23(11):2440–2446, 2017. 1

- [63] Noah Snavely. Photo tourism : Exploring image collections in 3d. *ACM Transactions on Graphics*, 2006. 2
- [64] Pratul P. Srinivasan, Boyang Deng, Xiuming Zhang, Matthew Tancik, Ben Mildenhall, and Jonathan T. Barron. Nerv: Neural reflectance and visibility fields for relighting and view synthesis. In *CVPR*, pages 7495–7504, 2021. 2, 3
- [65] Roman Suvorov, Elizaveta Logacheva, Anton Mashikhin, Anastasia Remizova, Arsenii Ashukha, Aleksei Silvestrov, Naejin Kong, Harshith Goka, Kiwoong Park, and Victor Lempitsky. Resolution-robust large mask inpainting with fourier convolutions. In *WACV*, pages 2149–2159, 2022. 1
- [66] Masaki Takeuchi, Hiroki Kusuyama, Daisuke Iwai, and Kosuke Sato. Projection mapping under environmental lighting by replacing room lights with heterogeneous projectors. *IEEE TVCG*, 30(5):2151–2161, 2024. 1
- [67] Takuro Takezawa, Daisuke Iwai, Kosuke Sato, Toshihiro Hara, Yusaku Takeda, and Kenji Murase. Material surface reproduction and perceptual deformation with projection mapping for car interior design. In *IEEE VR*, pages 251–258, 2019. 1
- [68] Matias Turkulainen, Xuqian Ren, Iaroslav Melekhov, Otto Seiskari, Esa Rahtu, and Juho Kannala. Dn-splatter: Depth and normal priors for gaussian splatting and meshing. *arXiv preprint arXiv:2403.17822*, 2024. 3
- [69] Atsuya Ueno, Toshiyuki Amano, and Chisato Yamauchi. Geometric calibration with multi-viewpoints for multi-projector systems on arbitrary shapes using homography and pixel maps. In *IEEE VRW*, pages 828–829, 2022. 1, 2
- [70] Jiaping Wang, Yue Dong, Xin Tong, Zhouchen Lin, and Baining Guo. Kernel nystrom method for light transport. In *SIGGRAPH*, New York, NY, USA, 2009. ACM. 2
- [71] Peng Wang, Lingjie Liu, Yuan Liu, Christian Theobalt, Taku Komura, and Wenping Wang. Neus: Learning neural implicit surfaces by volume rendering for multi-view reconstruction. In *NeurIPS*, pages 27171–27183. Curran Associates, Inc., 2021. 5
- [72] Yuxi Wang, Haibin Ling, and Bingyao Huang. Compenhr: Efficient full compensation for high-resolution projector. In *IEEE VR*, pages 135–145, 2023. 1, 3
- [73] Yuxi Wang, Haibin Ling, and Bingyao Huang. Vicomp: Video compensation for projector-camera systems. *IEEE TVCG*, 30(5):2347–2356, 2024. 1, 3
- [74] Gordon Wetzstein and Oliver Bimber. Radiometric compensation through inverse light transport. Technical report, Junior-Professor Augmented Reality, 2007. 1, 2, 3
- [75] Simon Willi and Anselm Grundhöfer. Robust geometric self-calibration of generic multi-projector camera systems. In *IEEE ISMAR*, pages 42–51, 2017. 1, 2
- [76] Yicheng Wu, Vivek Boominathan, Xuan Zhao, Jacob T Robinson, Hiroshi Kawasaki, Aswin Sankaranarayanan, and Ashok Veeraraghavan. Freecam3d: Snapshot structured light 3d with freely-moving cameras. In *ECCV*, pages 309–325. Springer, 2020. 1
- [77] Qiangeng Xu, Zexiang Xu, Julien Philip, Sai Bi, Zhixin Shu, Kalyan Sunkavalli, and Ulrich Neumann. Point-nerf: Point-based neural radiance fields. In *CVPR*, pages 5438–5448, 2022. 3
- [78] Shuntaro Yamazaki, Masaaki Mochimaru, and Takeo Kanade. Simultaneous self-calibration of a projector and a camera using structured light. In *CVPR 2011 WORKSHOPS*, pages 60–67, 2011. 1, 2
- [79] Yao Yao, Jingyang Zhang, Jingbo Liu, Yihang Qu, Tian Fang, David McKinnon, Yanghai Tsin, and Long Quan. Neirlf: Neural incident light field for physically-based material estimation. In *ECCV*, pages 700–716, Cham, 2022. Springer Nature Switzerland. 5
- [80] Mulin Yu, Tao Lu, Linning Xu, Lihan Jiang, Yuanbo Xiangli, and Bo Dai. Gsd: 3dgs meets sdf for improved rendering and reconstruction. *arXiv preprint arXiv:2403.16964*, 2024. 3
- [81] Zehao Yu, Torsten Sattler, and Andreas Geiger. Gaussian opacity fields: Efficient and compact surface reconstruction in unbounded scenes. *arXiv preprint arXiv:2404.10772*, 2024. 3
- [82] Richard Zhang, Phillip Isola, Alexei A Efros, Eli Shechtman, and Oliver Wang. The unreasonable effectiveness of deep features as a perceptual metric. In *CVPR*, pages 586–595, 2018. 6
- [83] Xiuming Zhang, Pratul P. Srinivasan, Boyang Deng, Paul Debevec, William T. Freeman, and Jonathan T. Barron. Nerfactor: neural factorization of shape and reflectance under an unknown illumination. *ACM Trans. Graph.*, 40(6), 2021. 2, 3

GS-ProCams: Gaussian Splatting-based Projector-Camera Systems

Supplementary Material

In the supplementary material, we provide a detailed description of the real-world data acquisition process in Appendix A, further implementation details of GS-ProCams in Appendix B, and additional qualitative results from experiments on ProCams simulation and projector compensation in Appendix C.

A. Real-world data acquisition

We use an RGB camera to acquire data in indoor lighting environments. Since a fixed projector typically illuminates a specific region of the target, we randomly position multiple camera viewpoints along the hemispherical surface surrounding the target and capture data sequentially.

We employ the pinhole camera model to represent both the projector and the camera viewpoints. A digital speckle pattern as illustrated in Fig. 9 is projected for each viewpoint, enabling us to obtain the locations and rotations of the projector and the camera viewpoints using COLMAP [58]. When applying the trained GS-ProCams to a previously unseen viewpoint, we only need to capture an image from this viewpoint with the same projection and then register it into the existing COLMAP model.

B. Implementation details

B.1. BRDF modeling

We use a simplified Disney BRDF model [8] to approximate the BRDF f . Specifically, the BRDF f is composed of a diffuse term $f_d = \frac{B}{\pi}$ and a specular term:

$$f_s(\omega_o, \omega_p) = \frac{DFG}{4(\mathbf{N} \cdot \omega_p) \cdot (\mathbf{N} \cdot \omega_o)}, \quad (18)$$

where D , F , and G denote the microfacet distribution function, Fresnel reflection and geometry factor. Define the half vector between ω_o and ω_p as \mathbf{h} , the normal distribution function D is evaluated as follows:

$$D = \frac{R^4}{\pi((\mathbf{N} \cdot \mathbf{h})^2(R^4 - 1) + 1)^2}, \quad (19)$$

and the Fresnel reflection term is approximated as:

$$F = 0.04 + (1 - 0.04)2^{(-5.55473(\omega_o \cdot \mathbf{h}) - 6.98316)(\omega_o \cdot \mathbf{h})}. \quad (20)$$

Define $k = \frac{(R+1)^2}{8}$, the geometry factor is given by:

$$G = \frac{(\mathbf{N} \cdot \omega_p)(\mathbf{N} \cdot \omega_o)}{(\mathbf{N} \cdot \omega_p \cdot (1 - k) + k)(\mathbf{N} \cdot \omega_o \cdot (1 - k) + k)}. \quad (21)$$

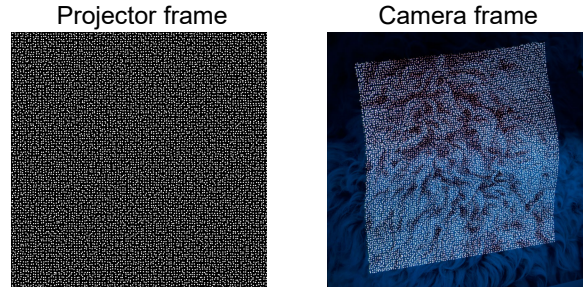


Figure 9. **Images registration.** We projected a fixed pattern (left) and captured an image using the camera (right) for each viewpoint, thereby determining the positions of the projector and camera viewpoints, using COLMAP [58].

B.2. Applications

As the principal manuscript outlines, our approach constitutes an efficient and fully differentiable framework for ProCams applications. In this section, we provide further details regarding the implementation.

Projector compensation. Our method facilitates view-agnostic projector compensation, as demonstrated in our experiments. Once the ProCams simulation is completed, GS-ProCams represents projector compensation as an inverse rendering problem. Given the desired appearance in the camera frame as \mathbf{I}_d , our framework allows for optimizing a virtual projector input pattern $\hat{\mathbf{I}}_p$ to make the simulation result $\hat{\mathbf{I}}_c$ in the virtual space align with \mathbf{I}_d as following:

$$\hat{\mathbf{I}}_p^* = \arg \min_{\hat{\mathbf{I}}_p} \mathcal{L}(\hat{\mathbf{I}}_c, \mathbf{I}_d), \quad (22)$$

where $\hat{\mathbf{I}}_p^*$ is the compensated projector input for the desired visual display effect.

More applications. We present some additional applications of GS-ProCams as shown in Fig. 1, such as projection-based diminished reality and text-driven projection mapping, which are achieved by integrating GS-ProCams with popular large generative models. Specifically, for projection-based diminished reality, we eliminate objects captured in the camera frame using an inpainting model [65] and then apply the techniques as described in Appendix B.2 to obtain the projector input pattern, which can act on reality to remove the target objects visually. Similarly, we capture the base appearance of a target from a specific viewpoint, and then we can use text prompts to drive diffusion models [21, 53] for text-driven projection mapping. It is precisely because GS-ProCams efficiently mod-

els view-agnostic geometric and photometric mappings of ProCams that it can facilitate the application of ProCams in reality.

C. More results

We present additional qualitative results of ProCams simulation and projector compensation with novel projections under novel viewpoints that GS-ProCams has not seen previously. Additional visual comparisons of ProCams simulation on the Nepmap synthetic dataset [14] are shown in Fig. 10. Additional visual comparisons of ProCams simulation on real-world benchmark dataset are given in Fig. 12. Additional comparisons of projector compensation on real-world benchmark dataset are provided in Fig. 11. Please note that the presented results are based on a novel viewpoint and a novel projection that GS-ProCams has not seen before within each trained scene.

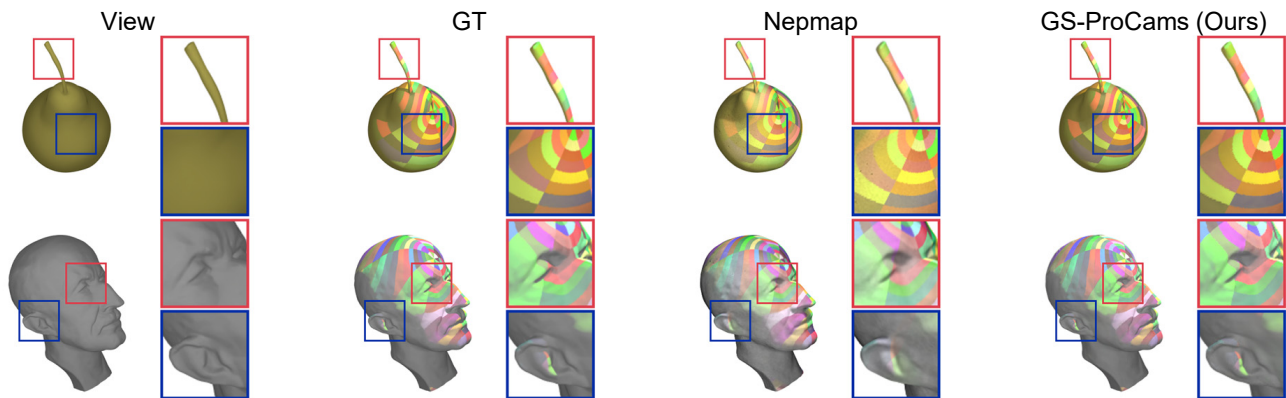


Figure 10. **Additional visual comparisons of ProCams simulation on the Nepmap synthetic dataset.** The first column displays an object from a novel viewpoint, the second column shows the object under a novel projection pattern, and the third and fourth columns present the results of two methods.

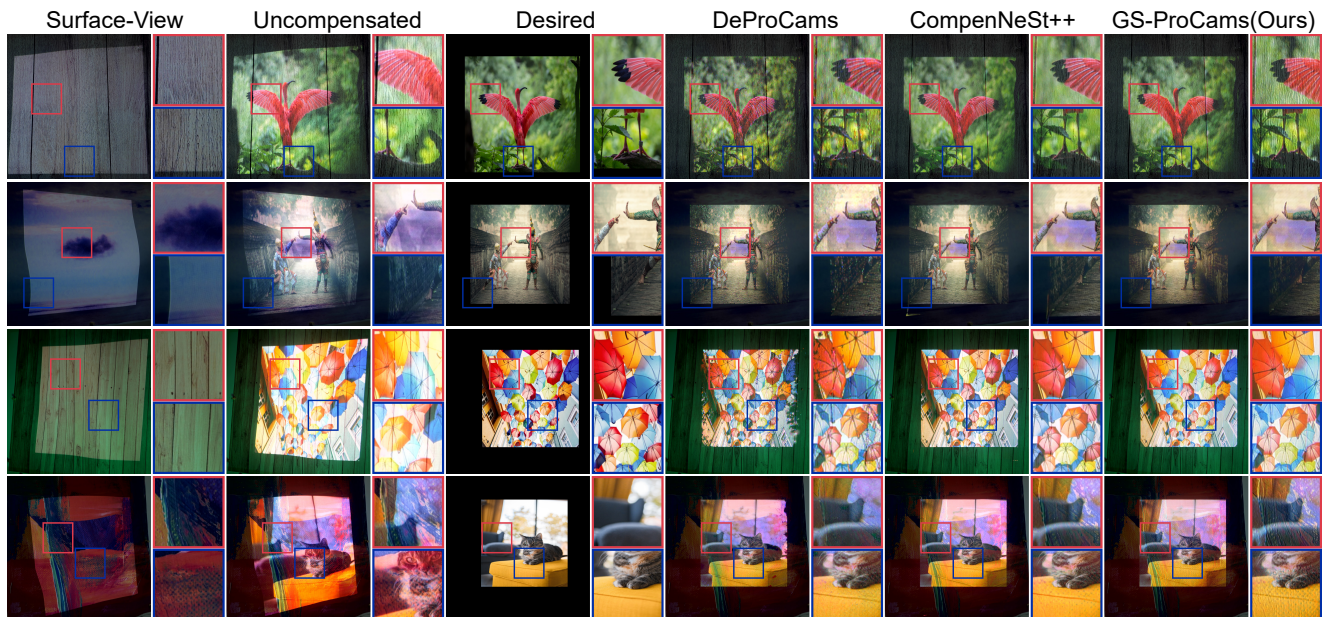


Figure 11. **Additional visual comparisons of projector compensation on real-world benchmark dataset.** Each row illustrates the results of a scene under a novel viewpoint that our proposed GS-ProCams has not previously seen. The other two view-specific methods necessitate repeated data capturing and training for these viewpoints. The first three columns respectively illustrate the surface appearance from the specified viewpoint, the uncompensated appearance, and the expected appearance. The last three columns display the compensated results from different models.

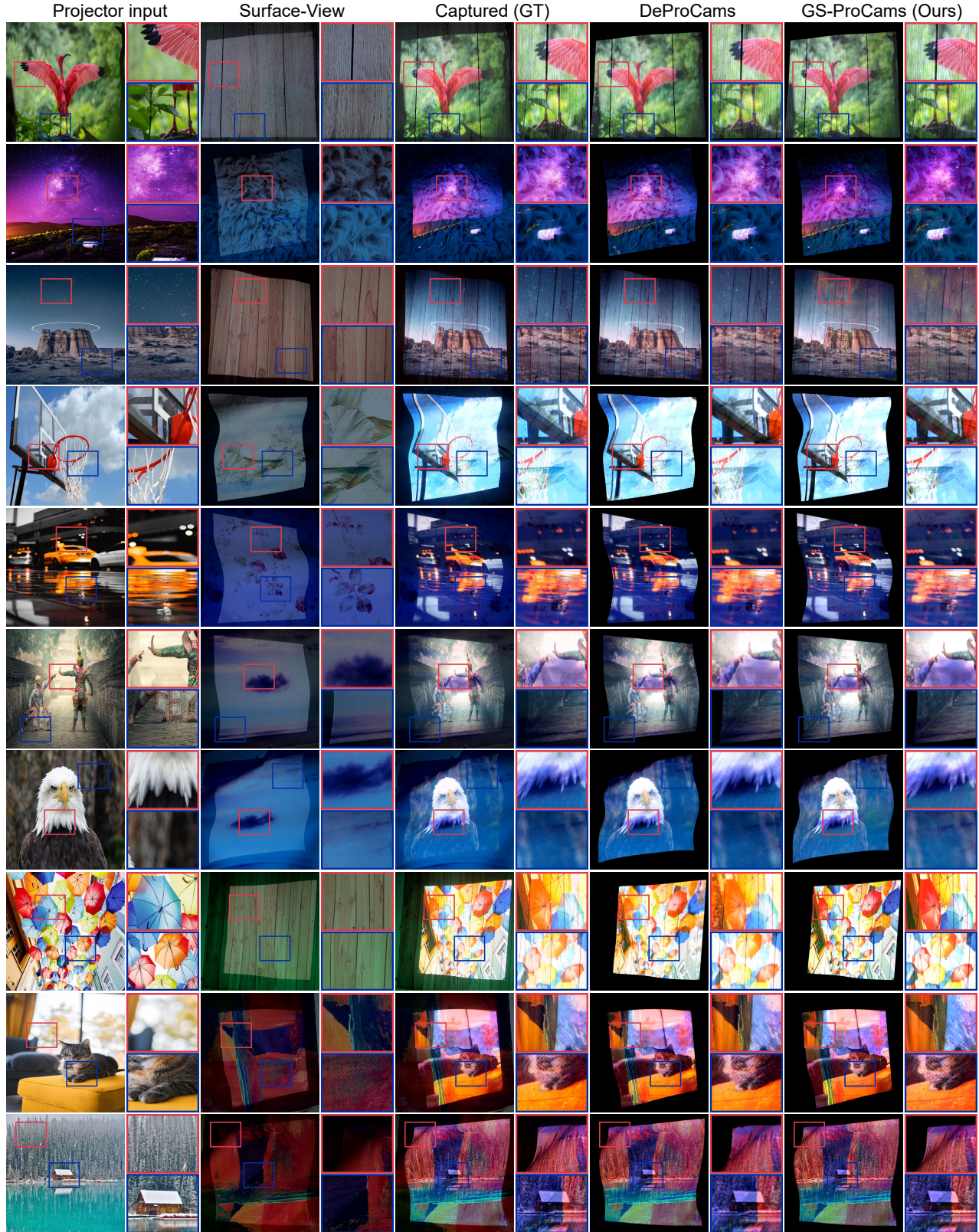


Figure 12. Additional visual comparisons of ProCams simulation on real-world benchmark dataset. Each row illustrates the results of a target surface under a novel viewpoint that our proposed GS-ProCams has not previously seen, while DeProCams has retrained for it.